Surface chemistry, film morphology, local electrochemical behavior and cytotoxic response of anodized AZ31B magnesium alloy

Leandro Antonio de Oliveira[1], Rejane Maria Pereira da Silva[2], Andrea Cecilia Dorion Rodas[1], Ricardo M. Souto[3], Renato Altobelli Antunes[1]

[1]Centro de Engenharia, Modelagem e Ciências Sociais Aplicadas (CECS), Universidade Federal do ABC (UFABC), 09210-580, Santo André – Brazil
[2]Instituto de Pesquisas Energéticas e Nucleares - IPEN/CNEN - Av. Prof. Lineu Prestes, 2242, São Paulo – Brazil
[3]Department of Chemistry, University of La Laguna, P.O. Box 456, 38200 La Laguna, Tenerife – Spain

Abstract

In this work, we provide a detailed investigation on the correlation between the surface chemistry, film morphology, global and local electrochemical behavior of the AZ31B alloy anodized under different constant current densities. The anodizing treatment was carried out in 1.0 M NaOH and 0.5 M Na_2SiO_3 solution, using three different current densities, 5 $mA.cm^{-2}$, 10 $mA.cm^{-2}$ and 20 $mA.cm^{-2}$. The surface morphology and thickness of the anodized layers were examined by scanning electron microscopy. The surface chemical states were assessed by X-ray photoelectron spectroscopy. The global electrochemical behavior was investigated by electrochemical impedance spectroscopy and potentiodynamic polarization. The local electrochemical activity was monitored by scanning electrochemical microscopy and scanning Kelvin probe. In vitro biocompatibility was assessed by cytotoxicity tests. The results indicated a marked influence of the anodizing current density on the surface morphology and global electrochemical behavior of the treated samples. The surface chemistry, in turn, was little affected by this parameter. The best corrosion resistance was obtained for the samples anodized at 20 $mA.cm^{-2}$.

Keywords: AZ31B, magnesium, anodizing, SECM, SKP

1. Introduction

Magnesium alloys have attracted considerable interest as important candidates for bioresorbable implant applications. Since they biodegrade via corrosion reactions in the human body a second surgery is not needed to remove them after the healing process is completed, which is expensive for the health care system and dangerous for the patient [1–8].

However, the main shortcoming of using these materials as temporary implant devices is its high degradation rate, which leads to hydrogen gas cavities [5,9,10]. Additionally, magnesium alloys suffer severe local corrosion attack, implying in premature loss of mechanical integrity, thus hindering their further clinical use especially in orthopaedical and cardiac applications [4,11–13].

Actually, 1.081 liters of H_2 are released from 1g of corroded Mg [14]. Fortunately, there are several possibilities of controlling the corrosion rate, such as alloying, mechanical preprocessing and surface modifications [1,15,16].

Anodization is an electrolytic oxidation process in which the metal (anode) is converted to an oxide film having desirable corrosion protective and functional properties [17–22]. The treatment promotes an increase in the film thickness, hardness, wear resistance, and better biocompatibility than the bare metal [3,19].

Extensive investigations have been performed to study the effects of the electrolyte composition, treatment time, electric parameters, post and pre-treatments on the properties of the anodized film [17,23–29]. The anodizing conditions have a deep influence on its composition and morphology. Thus, the search for an appropriate set of these parameters, which interact with each other, is necessary to obtain a film with the desired functionalities.

While global electrochemical tests have been applied to investigate the average corrosion activity, scanning probe techniques with enhance spatial resolution allow a comprehensive understanding of local corrosion processes at electrochemically active sites. Among these analytical probe techniques, scanning electrochemical microscopy (SECM) and scanning Kelvin probe (SKP) have been successfully used to characterize localized corrosion processes of different metallic materials, such as aluminum alloys [30–32] and steels [33–35]. Degradation of magnesium alloys at a microscopic level has also been reported [36–41]. Notwithstanding, the assessment of local corrosion spots of anodized layers produced on magnesium alloys by combining SECM and SKP are scarcely reported in the current literature.

In this study, we investigate the potentiality of anodization to control the dissolution rate of magnesium alloy in a simulated biological environment. The main focus is to study the correlation between film morphology, the chemical composition of the anodized layers and their global and local electrochemical behavior. The use of SECM and SKP to probe the local corrosion spots of anodized layers of magnesium alloys and the correlation between this information with the surface chemistry and global electrochemical response are rarely in the current literature. Furthermore, the *in vitro* biocompatibility was assessed by cytotoxicity tests.

2. Material and methods

2.1. Material and sample preparation

Hot rolled AZ31B magnesium alloy sheet (composition in wt.%: Al 2.54%, Zn 1.08%, Mn 0.38% and Mg balance), provided by Xi'an Yuechen Metal Products Co. Ltd., China was used as the substrate for the anodization process. Rectangular pieces were cut from the as-received sheet using a cut-off saw, obtaining dimensions of 10 mm x 10 mm x 3.5 mm. The specimens were connected to a copper wire in one side and then embedded in epoxy resin mounted in a PVC holder, leaving an average area of 1 cm^2 as the working surface. The surfaces were sequentially ground using waterproof silicon carbide paper (from #220 to #2400 grit size), polished using diamond paste (1 μm) and cleaned using deionized water and ethanol, being subsequently dried in a warm air stream provided by a conventional heat gun.

2.2. Anodizing treatment

The anodization process was carried out by high voltage DC power supply (MP5003D, 50-500V, 0-3A). The experiments were performed in an aqueous solution consisting of a mixture of 1.0 M NaOH and 0.5 M Na_2SiO_3. The AZ31B magnesium alloy was used as the anode while the stainless steel container was used as the cathode. The anodizing treatment was carried out at three different constant current densities 5 mA/cm^2, 10 mA/cm^2 and 20 mA/cm^2 for 5 minutes at room temperature. Then, the anodized samples were rinsed with deionized water and dried in air.

2.3. Film characterization

2.3.1. Morphology, roughness and chemical composition

The surface and cross-section morphologies were examined using scanning electron microscopy (SEM – JSM-6010LA, Jeol). Confocal laser scanning microscope (CLSM – LEXT OLS4100, Olympus) was used to determine the surface roughness. The R_a parameter was employed to quantify the roughness values.

XPS analyses were performed to investigate the chemical composition of the anodized films. The XPS spectra were acquired using a ThermoFisher Scientific K-Alpha$^+$ spectrometer with a monochromated Al K-α X-ray source. The energy scale was calibrated with respect to the adventitious C1s peak at 284.8 eV. High resolution spectra for the Mg2p, Si2p and O1s regions were obtained to assess the surface chemical states. The spectra were deconvoluted by curve-fitting using the *Smart* baseline for background subtraction in the Avantage^{TM} software.

2.3.2. Electrochemical behavior

2.3.2.1. Conventional electrochemical tests

The global electrochemical measurements were assessed in a potentiostat/galvanostat (M101, Autolab) using a typical three-electrode cell configuration. The test cell consisted of Ag/AgCl (KCl 3 M saturated) as the reference, a platinum wire as the counter electrode and the treated AZ31B alloy as the working electrode. The tests were conducted in a phosphate buffered saline (PBS), which contains: 0.355 g/L NaH_2PO_4+H_2O, 8.2 g/L NaCl, 0.105 g/L Na_2HPO_4 (anhydrous). The solution was prepared with deionized water and analytical grade reagents. Initially, the open circuit potential (OCP) was monitored for 1 h. Immediately, the samples were subjected to electrochemical impedance spectroscopy (EIS) at the OCP using 10 mV of AC voltage amplitude in a range of 100 kHz to 0.1 Hz. Right after, potentiodynamic polarization tests were carried out in a potential range from -500 mV (vs. OCP) to 0 $V_{Ag/AgCl}$ at a scanning rate of 1 $mV.s^{-1}$. Experiments were performed in triplicate.

The porosity degree of the anodized AZ31B alloy was estimated using an electrochemical method based on the use of Equation 1 [42,43]:

$$P = \left(\frac{R_{p,s}}{R_p}\right) x\ 10^{|\Delta E_{corr}|/b_a} \quad (1)$$

This method consists in the variation of the corrosion potential ($\Delta E_{corr} = E_{corr,substrate} - E_{corr,substrate+coating}$) caused by the presence of the anodized layer and from individual measurements of the polarization resistance (R_p) of the polished and anodized AZ31B.

Where $R_{p,s}$ denotes the polarization resistance of the polished substrate and R_p is the polarization resistance of the anodized substrate, while b_a is the anodic Tafel slope of the bare substrate. $R_{p,s}$ and b_a are determined from separate measurements of the polished substrate. The values of Rp were obtained from the potentiodynamic polarization curves.

2.3.2.2. Local corrosion techniques

A scanning electrochemical microscope (SECM) built by Sensolytics (GmbH Bochum, Germany) was used to evaluate the local corrosion process on the AZ31B alloy surface. A three electrode configuration was employed, with a 25 µm Pt disk ultra-micro-electrode (UME) as working electrode, Pt as counter-electrode (CE) and Ag/AgCl (KCl 3M saturated) as reference electrode (RE) was employed to complete the electrochemical cell.

Measurements were made at room temperature and with the substrate at the open circuit potential (unbiased). The AZ31B alloy was cut into strips and then embedded in epoxy resin to expose a working area of approximately 0.25 cm^2. The experiments were performed at selected heights of the tip above the surface. The operating height was set after recording *z*-approach curves, with the tip adjusted to ~10 µm above the surface. All experiments were performed using the surface generation/tip collection (SG/TC) mode. In the SG/TC mode, H_2 generation from corrosion of magnesium alloy was sensed in an oxidation reaction at the UME probe potential of 0.0 V versus Ag/AgCl (Equation 2).

$$H_2 \rightarrow 2H^+ + 2e^- \qquad (Reaction\ at\ the\ UME) \tag{2}$$

SECM maps in constant height mode were obtained by scanning the UME tip in the x-y plane and recording the tip current as a function of its location. The maps were recorded after 30 minutes of immersion in PBS solution. A working area of 400 µm x 200 µm was examined.

Scanning Kelvin Probe (SKP) measures the Volta potential difference between the working electrode and the probe, which vibrates above the surface sample in air. It is a non-contact and non-destructive technique. Both surfaces generate a capacitor and according to the probe vibration and its local variation, an AC current is generated. The amplitude of this current is directly proportional to the Volta potential difference. Thus,

the result enables to distinguish anode and cathode regions. Further, the SKP offers additional supportive information in the investigations of local corrosion processes.

The SKP experiments were operated in an electrochemical scanning system (AMETEK, VersaScan, USA) at room temperature in air. The distance between the probe tip and the specimen surface was maintained at 100 μm ± 10 μm throughout the tests, thus avoiding potential fluctuation stemming from the change in distance. A scanning step of 200 μm and 500 μm were used for x-y, respectively. The scans were acquired over a 3 mm x 6 mm region.

2.3.3. *In-vitro* biocompatibility

The 3T3/NIH (murine fibroblasts) cells were employed for cytotoxicity analysis. Cells were maintained on a regular feeding regime in a cell culture incubator at 37°C/5% CO_2/95% air atmosphere for 72 h. The culture media was DMEM supplemented with 10% fetal bovine serum and 1% antibiotic/antimycotic solution. The samples were immersed in the cellular medium at final concentration of 6 cm^2/mL. The cell viability samples were evaluated using the Methyl Tetrazolium (MTS) assay in 96 well plates. Liquid extracts were added into wells containing 3T3/NIH cells in culture medium. The MTS assay was then added and the cultures were reincubated for further 2 h (37 °C/5% CO_2). Next, the cultures were removed from the incubator and the absorbance was measured at a wavelength of 490 nm. A sterile medium was used as a control, and the cells were assumed to have metabolic activities of 100% in normal medium culture. The cell viability was calculated as follows (Eq. 3):

$$Cell\ viability = \frac{OD_{Sample}}{OD_{Control}}\ x\ 100 \qquad (3)$$

Where OD_{Sample} = optical density of the sample and $OD_{control}$ = optical density of the control.

3. Results and discussion

3.1. Morphological and topographical aspects of the anodized layers

SEM micrographs of the top surfaces of the AZ31B alloy in the polished and anodized conditions are shown in Fig. 1. The polished surface presents small white-colored precipitates whose composition is mainly comprised of Al and Mn as confirmed by EDS analysis (Fig. 2). Similar findings are reported by other authors [44]. After

anodization, the surface topography is altered. The anodized layer completely covered the substrate independently of the current dentisy. The compactness of the surface film, in turn, was affected by this parameter. As seen in Fig. 1b the film formed over the 5 $mA.cm^{-2}$ sample is discontinuously distributed throughout the surface, showing several cracks. These features are less marked when the anodizing current was increased to 10 $mA.cm^{-2}$ (Fig. 1c). The surface obtained at 20 $mA.cm^{-2}$ (Fig. 1d) is the most compact one. Similar results were reported by Chai et al. [25]. The anodized layer became more compact as the current density was raised from 5 to 20 $mA.cm^{-2}$.

Figure 1

Figure 2

As the thickness of the anodic film may greatly affect its corrosion protection ability, the cross-sections of the anodized samples were examined by SEM. The results are shown in Fig. 3. The film obtained at 5 $mA.cm^{-2}$ (Fig. 3a) is the thinnest one, reaching approximately 1 µm. By increasing the current density, the thickness of the resulting layer was markdly raised at 10 $mA.cm^{-2}$ (Fig. 3b). The increasing trend was not kept, though, when the current density was raised to 20 $mA.cm^{-2}$ (Fig. 3c). Notwithstanding, the interface between the substrate and the anodic layer became more homogeneous than for the film produced at 10 $mA.cm^{-2}$ which can be beneficial to the barrier properties against electrolyte penetration.

Figure 3

Further evaluation of the topograpical features of the anodized layers was carried out by confocal laser scanning microscopy (CLSM). The average roughness (Ra) was, therefore, determined from CLSM micrographs shown in Fig. 4. Representative transverse profiles of the scanned lines across the sample surface are also presented. The Ra values are displayed in Table 1. The anodized films presented an obvious increase of the Ra values with respect to the polished condition. As shown in Table 1, the increase of the anodizing current density did not affect the average roughness of the anodic film, since the Ra values are very similar for all anodized layers. El Mahallawy et al. [45] reported that the surface roughness of the anodized layer formed on the AZ91 magnesium alloy increased with the current density and the thickness of the anodic film. In the present work, in spite of the increased film thickness when the current density was raised from 5 $mA.cm^{-2}$ to 10 $mA.cm^{-2}$, the average roughness was not significantly affected. The same occurred for the film obtained at 20 $mA.cm^{-2}$. Cely et al. [46], in turn, reported only a marginal effect of the current density on the average roughness of

anodic layers formed on Ti6Al4V. According to El Mahallawy et al. [45] surface roughness is also affected by the pores and cracks in the anodic film.

Figure 3

Table 1

3.2. Surface chemistry

XPS survey spectra of the polished and anodized samples are shown in Fig. 5. The main elements in the anodic films are Mg, Si, Na and O. The presence of Al was detected only in the polished sample as it is part of the naturally formed oxide film on the surface of the AZ31B alloy. Si and Na were not detected in the polished alloy, since these elements are incorporated by exposition to the anodizing electrolyte. Detailed information about the surface chemical states of the anodized layers was achieved by acquiring the XPS high resolution spectra for the Mg1s, Si2p and O1s regions.

The Mg1s core level for the 20 $mA.cm^{-2}$ sample is shown in Fig. 6. The spectra for the 5 $mA.cm^{-2}$ and 10 $mA.cm^{-2}$ (not shown) are very similar. The spectrum was deconvoluted into two components. The one at 1303.3 eV is ascribed to $Mg(OH)_2$ [47] whereas the highest binding energy (1304.2 eV) component is assigned to Mg_2SiO_4 [48]. Magnesium hydroxide is the dominant species, but the anodic film consists of a mixture of $Mg(OH)_2$ and Mg_2SiO_4, independently of the current density employed during anodization. The formation of such species during anodization of magnesium alloys is in accordance with the literature, being related to the following reactions [49]:

$$Mg^{2+} + 2e \rightarrow Mg(OH)_2 \quad (4)$$

$$Mg^{2+} + SiO_3^{2-} + OH^- \rightarrow Mg_2SiO_4 + H_2O \quad (5)$$

Figure 6

The Si2p core leves for the anodized samples are shown in Fig. 7. The fitting parameters are displayed in Table 2. The spectrum for the sample anodized at 5 $mA.cm^{-2}$ was deconvoluted into two components. The low binding energy one was assigned to silicate species (Mg_2SiO_4) whereas the high binding energy component was due to silica-type bonds (SiO_2) [48,50]. Silica bonds predominate over silicate, as seen in Tab. 2. The formation of SiO_2 can take place due to the reaction between magnesium ions and silicate anions, according to equation (6) [17]:

$$Mg^{2+} + SiO_3^{2-} \rightarrow Mg_2SiO_4 + SiO_2 \quad (6)$$

Figure 7

Table 2

The Si2p core levels for the samples anodized at 10 mA.cm^{-2} and 20 mA.cm^{-2} shows one single component which was assigned to silicate-type species. These results point that reaction (5) is favored by increasing the current density of the anodizing process.

Figure 8 shows the O1s core levels for the anodized samples. The spectra were deconvoluted into two components, independently of the current density employed during anodization. A third component at approximately 535 eV is also found in all spectra. It is due to an Auger peak of sodium (NaKLL), revealing that sodium species are adsorbed on the sample surface during anodization in the mixed NaOH/Na_2SiO_3 electrolyte, in accordance with the results shown in the survey spectra (Figure 5). The component at the lowest binding energy is assigned to O^{2-} species such as Mg_2SiO_4 whereas the highest binding energy component is assigned to hydroxide species such as $Mg(OH)_2$. These species were found in the Mg1s core levels, confirming that the anodic layers mainly consist of a mixture of Mg_2SiO_4 and $Mg(OH)_2$, being SiO_2 also part of the film obtained at 5 mA.cm^{-2}.

Figure 8

3.3 Global electrochemical tests

3.3.1 Electrochemical impedance spectroscopy (EIS)

Nyquist plots of the polished and anodized samples are shown in Fig. 9. Bode plots (phase angle vs. frequency and impedance modulus vs. frequency) are displayed in Fig. 10. The results were obtained after 1 h of immersion in PBS at room temperature.

Figure 9

The Nyquist plots are characterized by flattened capacitive loops whose diameter increased after anodizing. The diameter of the capactive loop is associated with the charge transfer resistance, being related to the corrosion resistance of the electrode in solution [51]. The polished sample presented the lowest impedance values, indicating the poor protective character of the naturally formed oxide film on its surface. Anodization promoted an increase of the corrosion resistance as denoted by the significant impedance rise with respect to the polished sample. The anodized layer obtained at 20 mA.cm^{-2} shows the highest impedance values, suggesting it presents the most protective surface.

Bode plots (Fig. 10) point to the same direction. The maximum phase angles of the anodized samples are more capacitive (-70°) than for the polished one (approximately -60°), as seen in Fig. 10a. Furthermore, the drop off of the phase angles occur at lower frequencies for the anodized samples, especially for the anodic film obtained at 20 $mA.cm^{-2}$. The resistive character of the electrode surface is, therefore, less marked for this condition, indicating its superior corrosion resistance when compared to the other anodized layers and the polished alloy.

Figure 10

Additional evidence for the superior corrosion resistance of the 20 $mA.cm^{-2}$ film is perceived from the log |Z| vs. frequency plots shown in Fig. 10b. It presents slightly higher impedance values at very low frequencies than the sample anodized at 10 $mA.cm^{-2}$. The polished condition is the least corrosion resistant, as indicated by its low impedance values. Moreover, the capacitive behavior associated with the typical -1 slope is lost at the highest frequencies for the polished condition, assuming a resistive character (impedance modulus almost independent of the applied frequency) near 10 Hz. The resistive behavior indicate that charge transfer reactions are taking place at the metal/electrolyte interface which is associted with a corroding surface [52,53]. This phemenon is delayed for the anodized samples, especially for the 20 $mA.cm^{-2}$ film, confirming its remarkable protective ability against electrolyte penetration and the onset of corrosion at the metal/anodic film interface.

3.3.2. Potentiodynamic polarization curves

Potentiodynamic polarization curves of the polished and anodized samples obtained in PBS at room temperature are shown in Fig. 11. The corrosion current densities (i_{corr}) and corrosion potentials (E_{corr}) were obtained from these curves, using the Tafel extrapolation method, considering only the cathodic branches. The values are displayed in Table 3.

Figure 11

Table 3

The corrosion potentials were not significantly altered by the anodization process. If one notices the standard deviation of the values shown in Table 3, E_{corr} can be considered similar for all conditions, both anodized and polished ones. The values of i_{corr}, in turn, markedly decreased after anodization. The results suggest that the anodized

layers were an effective barrier against electrolyte penetration. The i_{corr} values are similar, though, for all anodized samples. Thus, the effect of the anodizing current density on the overall corrosion rate of the coated AZ31B alloy is not clearly observed from these data. It is, therefore, important to examine the anodic branches of the polarization with more detail. It is seen that the anodic current densities of the films obtained at 10 $mA.cm^{-2}$ and 20 $mA.cm^{-2}$ are significantly lower than those of the polished sample. In addition, a small passivity region can be clearly seen for these samples which is absent from the curve of the polished surface. In this respect, the anodized layer effectively slowed down the corrosion process of the AZ31B alloy. The 20 $mA.cm^{-2}$ film presented the widest passive region and the lowest anodic current densities throghouth the whole potential range, thus indicating its better protective ability. These results confirm those obtained by EIS. Yet, it is noteworthy that the film obtained at 5 $mA.cm^{-2}$ presents only an incipient pseudo-passive region when compared to the anodic films produced at higher current densities. Moreover, the anodic current densities for this film are the highest among the anodized samples and even than those of the polished alloy.

The global electrochemical behavior of the anodized AZ31B alloy seems to be markedly affected by the morphological features shown in section 3.1 (Figure 1). According to Tab. 3, the porosity degree were strongly reduced for the anodized layers produced at 10 $mA.cm^{-2}$ (Fig. 1c) and 20 $mA.cm^{-2}$ (Fig. 1d), which is in agreement with their high impedance values (Figs. 9 and 10b), while the most stable passive region in the polarization curves is observed for the highest current density condition (Fig. 11). The porosity percentage is commonly associated with a function of the spark potential which, in turn, is a function of the applied current density [54–56]. Furthermore, when the current density rises, small sparks change into large ones, and it moves faster during the anodization process [25]. Thus, the molten oxide spreads more uniformly along the magnesium surface. This could be a reason for the decrease of the porosity percentage for those conditions. Whereas the conductivity to produce the anodized film at 5 $mA.cm^{-2}$, in turn, could be insufficient, which leads to a porous coating, and would assist a quicker penetration of the corrosive medium.

It is also important to observe that the surface chemistry of the anodized layers were very similar for all samples, as seen in section 3.2. In this respect, the current density of the anodizing treatment did not affect the chemical state of the species in the anodized

layer but deeply influences its morphology. This, in turn, play a prominent role on its overall corrosion resistance.

3.4. Local electrochemical behavior

The electrochemical behavior of the AZ31B in the polished and anodized conditions was further evaluated by scanning electrochemical microscopy (SECM). The UME detected the hydrogen oxidation reaction at a potential of 0 $V_{Ag/AgCl}$, as described in section 2.3.2. The substrate was kept unbiased. SECM 2D maps are shown in Fig. 12. The current scale at the right part of each one of the maps are related to the H_2 flux probed by the UME. Higher currents are associated with more intense H_2 generation at the surface of the AZ31B substrate and, thus, to a more intense corrosion process due to magnesium dissolution.

Figure 12

It is obvious that corrosion is much more intense at the surface of the polished alloy (Fig. 12a), as denoted by the high currents measured throughout the probed area. Anodization led to a significant decrease of the local current by blocking the access of the electrolyte to the underlying metallic substrate. The measured currents were reduced by almost two orders of magnitude after the anodizing treatment. They reach higher values for the 5 $mA.cm^{-2}$ film when compared to the samples anodized at higher current densities, as observed in Fig. 12b.

SECM is very sensitive to defects at coated surfaces [57]. The higher currents of the 10 $mA.cm^{-2}$ with respect to the 20 $mA.cm^{-2}$ condition suggest that the probed area present more spots where H_2 is being formed and, thus, the magnesium substrate corrodes. The local character of the technique is able to sense these species at small defective sites which can be probed by the UME while scanning the surface of the 20 $mA.cm^{-2}$. The heterogeneous nature of the anodized surface morphology can lead to variations of roughness and also to the presence of pores and microcracks over the treated surface. As such, the H_2 flux detected by the UME depends on these local imperfections. SECM is able to detect it accurately. Our results show that the local electrochemical response of the anodized layers agrees well with the global response obtained by EIS and potentiodynamic polarization and the sample anodized at 20 $mA.cm^{-2}$ presents the lowest electrochemical activity.

The surface potential distributions over the AZ31B alloy in the polished and in the anodized conditions were measured by Scanning Kelvin Probe (SKP). SKP 2D

maps are presented in Figure 13. The potential distribution is in agreement with the morphologies (Fig.1) and SECM results (Fig. 12). The surface Volta potential is related to the changes in electronic energy and the work function. Thus, higher potential is associated to an increased work function, hence, higher energy is required to remove an electron through the surface region [41]. The naturally formed oxide in the polished condition (Fig. 12a) presented a large potential difference between cathode and anode regions over its surface, assuming a very negative potential in the center of the map. This distinguishable potential variation act as a driving force for corrosion [58]. Meanwhile, the anodized layers show fewer negative potential spots and appeared to mitigate the larger potential difference over its surface film. As expected, the anodized film at 20 $mA.cm^{-2}$ showed nobler and more homogeneous potential distribution compared to the other films, confirming the tendency suggested by SECM (Fig. 12d).

Figure 13

3.5 In vitro biocompatibility

The *in vitro* biocompatibility of the AZ31B alloy in the polished and anodized conditions was evaluated by citotoxicity tests, taking into account the MTS metabolic activity assay. The cell viability results are shown in Fig. 14. Based on ISO 10993-5, the material is considered cytotoxic when the cell viability is below 70% [59]. Only the negative control (latex) was cytotoxic. The anodized samples were not cytotoxic. The highest cell viability was observed for the 20 $mA.cm^{-2}$ condition. It is possible to infer that this treatment provided the best mean to control the anodic dissolution rate of the AZ31B alloy without sacrificing its intrinsic biocompatibility.

Figure 14

4. Conclusions

Anodization of the AZ31B alloy in a mixed NaOH and Na_2SiO_3 solution was successfully accomplished in the constant current density mode. The surface morphology of the anodized layers was affected by the current density. The most compact layer was obtained at 20 $mA.cm^{-2}$. This, in turn, markedly affected the global electrochemical behavior of the AZ31B alloy. The highest corrosion resistance was obtained for the most compact layer. The anodized films were mainly comprised of a mixture of Mg_2SiO_4 and $Mg(OH)_2$. This composition was little affected by the current

density of the anodizing process. SECM was effective at probing the oxidation of H_2 species at the surface of the anodized samples and proved to be very sensitive to surface defects. SKP confirms the protective character against localized corrosion of the film anodized at 20 $mA.cm^{-2}$. The anodizing treatment did not alter the intrinsic *in vitro* biocompatibility of the AZ31B alloy. The results reveal that the current density is a relevant parameter to control the overall corrosion resistance of the AZ31B alloy.

Acknowledgements

The authors thank the Brazilian agencies FAPESP (Proc. 2015/22921-6) and CAPES (Finance code 001) for the financial support, and the Multiuser Experimental Facilities (UFABC) for the experimental support for this work.

References

[1] M.P. Staiger, A.M. Pietak, J. Huadmai, G. Dias, Magnesium and its alloys as orthopedic biomaterials: A review, Biomaterials. 27 (2006) 1728–1734. doi:10.1016/j.biomaterials.2005.10.003.

[2] R. Zeng, W. Dietzel, F. Witte, N. Hort, C. Blawert, Progress and challenge for magnesium alloys as biomaterials, Adv. Eng. Mater. 10 (2008) 3–14. doi:10.1002/adem.200800035.

[3] G. Song, Control of biodegradation of biocompatable magnesium alloys, Corros. Sci. 49 (2007) 1696–1701. doi:10.1016/j.corsci.2007.01.001.

[4] D. Zhao, F. Witte, F. Lu, J. Wang, J. Li, L. Qin, Current status on clinical applications of magnesium-based orthopaedic implants: A review from clinical translational perspective, Biomaterials. 112 (2017) 287–302. doi:10.1016/j.biomaterials.2016.10.017.

[5] F. Witte, Acta Biomaterialia The history of biodegradable magnesium implants : A review, Acta Biomater. 6 (2010) 1680–1692. doi:10.1016/j.actbio.2010.02.028.

[6] F. Feyerabend, H.-P. Wendel, B. Mihailova, S. Heidrich, N.A. Agha, U. Bismayer, R. Willumeit-Römer, Blood compatibility of magnesium and its alloys, Acta Biomater. 25 (2015) 384–394. doi:10.1016/j.actbio.2015.07.029.

[7] X. Li, X. Liu, S. Wu, K.W.K. Yeung, Y. Zheng, P.K. Chu, Design of magnesium alloys with controllable degradation for biomedical implants: From bulk to surface, Acta Biomater. 45 (2016) 2–30. doi:10.1016/j.actbio.2016.09.005.

[8] S. Agarwal, J. Curtin, B. Duffy, S. Jaiswal, Biodegradable magnesium alloys for orthopaedic applications: A review on corrosion, biocompatibility and surface modifications, Mater. Sci. Eng. C. 68 (2016) 948–963. doi:10.1016/j.msec.2016.06.020.

[9] F. Witte, V. Kaese, H. Haferkamp, E. Switzer, A. Meyer-Lindenberg, C.J. Wirth, H. Windhagen, In vivo corrosion of four magnesium alloys and the associated bone response, Biomaterials. 26 (2005) 3557–3563. doi:10.1016/j.biomaterials.2004.09.049.

[10] J. Kuhlmann, I. Bartsch, E. Willbold, S. Schuchardt, O. Holz, N. Hort, D. Höche, W.R. Heineman, F. Witte, Fast escape of hydrogen from gas cavities around corroding magnesium implants, Acta Biomater. 9 (2013) 8714–8721. doi:10.1016/j.actbio.2012.10.008.

[11] P. Wan, L. Tan, K. Yang, Surface Modification on Biodegradable Magnesium Alloys as Orthopedic Implant Materials to Improve the Bio-adaptability: A Review, J. Mater. Sci. Technol. 32 (2016) 827–834. doi:10.1016/j.jmst.2016.05.003.

[12] L. Tan, X. Yu, P. Wan, K. Yang, Biodegradable Materials for Bone Repairs: A Review, J. Mater. Sci. Technol. 29 (2013) 503–513. doi:10.1016/j.jmst.2013.03.002.

[13] L. Tan, Q. Wang, X. Lin, P. Wan, G. Zhang, Q. Zhang, K. Yang, Loss of mechanical properties in vivo and bone-implant interface strength of AZ31B magnesium alloy screws with Si-containing coating, Acta Biomater. 10 (2014) 2333–2340. doi:10.1016/j.actbio.2013.12.020.

[14] F. Witte, J. Fischer, J. Nellesen, C. Vogt, J. Vogt, T. Donath, F. Beckmann, In vivo corrosion and corrosion protection of magnesium alloy LAE442, Acta Biomater. 6 (2010) 1792–1799. doi:10.1016/j.actbio.2009.10.012.

[15] M. Pogorielov, E. Husak, A. Solodivnik, S. Zhdanov, Magnesium-based biodegradable alloys : Degradation , application , and alloying elements, 9 (2017) 27–38. doi:10.1556/1646.9.2017.04.

[16] H. Hornberger, S. Virtanen, A.R. Boccaccini, Biomedical coatings on magnesium alloys - A review, Acta Biomater. 8 (2012) 2442–2455.

doi:10.1016/j.actbio.2012.04.012.

[17] H. Fukuda, Y. Matsumoto, Effects of Na2SiO3 on anodization of Mg-Al-Zn alloy in 3 M KOH solution, Corros. Sci. 46 (2004) 2135–2142. doi:10.1016/j.corsci.2004.02.001.

[18] M. Santamaria, F. Di Quarto, S. Zanna, P. Marcus, The influence of surface treatment on the anodizing of magnesium in alkaline solution, Electrochim. Acta. 56 (2011) 10533–10542. doi:10.1016/j.electacta.2011.05.027.

[19] G.L. Song, Z. Shi, Corrosion mechanism and evaluation of anodized magnesium alloys, Corros. Sci. 85 (2014) 126–140. doi:10.1016/j.corsci.2014.04.008.

[20] C. Blawert, W. Dietzel, E. Ghali, G. Song, Anodizing treatments for magnesium alloys and their effect on corrosion resistance in various environments, Adv. Eng. Mater. 8 (2006) 511–533. doi:10.1002/adem.200500257.

[21] S. Hiromoto, A. Yamamoto, Control of degradation rate of bioabsorbable magnesium by anodization and steam treatment, Mater. Sci. Eng. C. 30 (2010) 1085–1093. doi:10.1016/j.msec.2010.06.001.

[22] D. Xue, Y. Yun, M.J. Schulz, V. Shanov, Corrosion protection of biodegradable magnesium implants using anodization, Mater. Sci. Eng. C. 31 (2011) 215–223. doi:10.1016/j.msec.2010.08.019.

[23] R.F. Zhang, D.Y. Shan, R.S. Chen, E.H. Han, Effects of electric parameters on properties of anodic coatings formed on magnesium alloys, Mater. Chem. Phys. 107 (2008) 356–363. doi:10.1016/j.matchemphys.2007.07.027.

[24] W. Ximei, Z. Liqun, L. Huicong, L. Weiping, Influence of surface pretreatment on the anodizing film of Mg alloy and the mechanism of the ultrasound during the pretreatment, Surf. Coatings Technol. 202 (2008) 4210–4217. doi:10.1016/j.surfcoat.2008.03.018.

[25] L. Chai, X. Yu, Z. Yang, Y. Wang, M. Okido, Anodizing of magnesium alloy AZ31 in alkaline solutions with silicate under continuous sparking, Corros. Sci. 50 (2008) 3274–3279. doi:10.1016/j.corsci.2008.08.038.

[26] V. Ezhilselvi, J. Nithin, J.N. Balaraju, S. Subramanian, The influence of current density on the morphology and corrosion properties of MAO coatings on AZ31B magnesium alloy, Surf. Coatings Technol. 288 (2016) 221–229. doi:10.1016/j.surfcoat.2016.01.040.

[27] A. Yabuki, M. Sakai, Anodic films formed on magnesium in organic, silicate-containing electrolytes, Corros. Sci. 51 (2009) 793–798.

doi:10.1016/j.corsci.2009.02.001.

[28] L. Zhu, Y. Li, W. Li, Influence of silica sol particle behavior on the magnesium anodizing process with different anions addition, Surf. Coatings Technol. 202 (2008) 5853–5857. doi:10.1016/j.surfcoat.2008.06.157.

[29] S.N. Pak, Z. Jiang, Z. Yao, J.M. Ju, K.S. Ju, U.J. Pak, Fabrication of environmentally friendly anti-corrosive composite coatings on AZ31B Mg alloy by plasma electrolytic oxidation and phytic acid/3-aminopropyltrimethoxysilane post treatment, Surf. Coatings Technol. 325 (2017) 579–587. doi:10.1016/j.surfcoat.2017.07.003.

[30] R. Maria, P. Silva, U. Donatus, M.X. Milagre, R.A. Antunes, I. Costa, The local electrochemical behavior of the AA2098 - T351 and surface preparation effects investigated by scanning electrochemical microscopy, (2019) 1–11. doi:10.1002/sia.6682.

[31] H. rong Zhou, X. gang Li, C. fang Dong, K. Xiao, T. Li, Corrosion behavior of aluminum alloys in Na2SO4solution using the scanning electrochemical microscopy technique, Int. J. Miner. Metall. Mater. 16 (2009) 84–88. doi:10.1016/S1674-4799(09)60014-5.

[32] S. Wang, H. Peng, Z. Shao, Q. Zhao, N. Du, Sealing of anodized aluminum with phytic acid solution, Surf. Coat. Technol. 286 (2016) 155–164. doi:10.1016/j.surfcoat.2015.12.024.

[33] S. González, J.J. Santana, Y. González-García, L. Fernández-Mérida, R.M. Souto, Scanning electrochemical microscopy for the investigation of localized degradation processes in coated metals: Effect of oxygen, Corros. Sci. 53 (2011) 1910–1915. doi:10.1016/j.corsci.2011.02.008.

[34] M.C.L. de Oliveira, V. Correa, R. Maria, N.B. De Lima, J.T.D. De Oliveira, L.A. de Oliveira, Structural, Adhesion and Electrochemical Characterization of Electroless Plated Ni-P- Carbon Black Composite Films on API 5L X80 Steel, (2019). doi:10.1007/s11665-019-04245-2.

[35] M. Rohwerder, F. Turcu, High-resolution Kelvin probe microscopy in corrosion science: Scanning Kelvin probe force microscopy (SKPFM) versus classical scanning Kelvin probe (SKP), Electrochim. Acta. 53 (2007) 290–299. doi:10.1016/j.electacta.2007.03.016.

[36] S.S. Jamali, S.E. Moulton, D.E. Tallman, M. Forsyth, J. Weber, A. Mirabedini, G.G. Wallace, Corrosion protection afforded by praseodymium conversion film

on Mg alloy AZNd in simulated biological fluid studied by scanning electrochemical microscopy, J. Electroanal. Chem. 739 (2015) 211–217. doi:10.1016/j.jelechem.2014.11.033.

[37] S.H. Salleh, S. Thomas, J.A. Yuwono, K. Venkatesan, N. Birbilis, Enhanced hydrogen evolution on Mg (OH)2covered Mg surfaces, Electrochim. Acta. 161 (2015) 144–152. doi:10.1016/j.electacta.2015.02.079.

[38] S. Thomas, O. Gharbi, S.H. Salleh, P. Volovitch, K. Ogle, N. Birbilis, On the effect of Fe concentration on Mg dissolution and activation studied using atomic emission spectroelectrochemistry and scanning electrochemical microscopy, Electrochim. Acta. 210 (2016) 271–284. doi:10.1016/j.electacta.2016.05.164.

[39] S.S. Jamali, S.E. Moulton, D.E. Tallman, Y. Zhao, J. Weber, G.G. Wallace, Self-healing characteristic of praseodymium conversion coating on AZNd Mg alloy studied by scanning electrochemical microscopy, Electrochem. Commun. 76 (2017) 6–9. doi:10.1016/j.elecom.2017.01.004.

[40] L.A. De Oliveira, R.A. Antunes, C. De Engenharia, Scanning Electrochemical Microscopy (SECM) Study of the Electrochemical Behavior of Anodized AZ31B Magnesium Alloy in Simulated Body Fluid, Mater. Res. 22 (2019).

[41] Y. Wang, J. Wang, J. Zhang, Z. Zhang, Effects of spark discharge on the anodic coatings on magnesium alloy, Mater. Lett. 60 (2006) 474–478. doi:10.1016/j.matlet.2005.09.015.

[42] L. Chenglong, Y. Dazhi, L. Guoqiang, Q. Min, Corrosion resistance and hemocompatibility of multilayered Ti/TiN-coated surgical AISI 316L stainless steel, Mater. Lett. 59 (2005) 3813–3819. doi:10.1016/j.matlet.2005.06.058.

[43] M.C.L. De Oliveira, V.S.M. Pereira, O.V. Correa, R.A. Antunes, Corrosion performance of anodized AZ91D magnesium alloy: Effect of the anodizing potential on the film structure and corrosion behavior, J. Mater. Eng. Perform. 23 (2014) 593–603. doi:10.1007/s11665-013-0755-0.

[44] A. Pardo, M.C. Merino, A.E. Coy, R. Arrabal, F. Viejo, E. Matykina, Corrosion behaviour of magnesium/aluminium alloys in 3.5 wt.% NaCl, Corros. Sci. 50 (2008) 823–834. doi:10.1016/j.corsci.2007.11.005.

[45] N.A. El Mahallawy, M.A. Shoeib, M.H. Abouelenain, AZ91 Magnesium Alloys : Anodizing of Using Environmental Friendly Electrolytes, 2011 (2011) 62–72. doi:10.4236/jsemat.2011.12010.

[46] M.M. Cely, A. Toro, H. Estupiñan, D.Y. Peña, Caracterización microestructural

y comportamiento tribológico de aleación ti6al4v anodizado . Microstructure characterization and tribological behavior of anodized ti6al4v alloy ., 305 (2014) 295–305.

[47] C. Man, C. Dong, Y. Fang, K. Xiao, C. Guo, G. He, X. Li, The Corrosion Behavior of Magnesium Alloy AZ31 in Hot and Dry Atmospheric Environment in Turpan , China, 10 (2015) 8691–8705.

[48] Q. Wang, L. Tan, K. Yang, Q. Wang, L. Tan, K. Yang, Preparation and in vitro degradation characterization of Si-containing coating on AZ31B alloy Preparation and in vitro degradation characterization of Si-containing coating on AZ31B alloy, Mater. Technol. 7857 (2016) 1–8. doi:10.1080/10667857.2016.1254402.

[49] G.B. Darband, M. Aliofkhazraei, P. Hamghalam, N. Valizade, Plasma electrolytic oxidation of magnesium and its alloys : Mechanism , properties and applications, J. Magnes. Alloy. 5 (2017) 74–132. doi:10.1016/j.jma.2017.02.004.

[50] Z.J. Li, Y. Yuan, X.Y. Jing, Comparison of plasma electrolytic oxidation coatings on Mg – Li alloy formed in molybdate / silicate and aluminate / silicate composite electrolytes, (2014) 26–28. doi:10.1002/maco.201206652.

[51] B.M.F. Pérez, J.A.G. Guzmán, S. González, R.M. Souto, Electrochemical Impedance Spectroscopy Investigation of the Corrosion Resistance of a Waterborne Acrylic Coating Containing Active Electrochemical Pigments for the Protection of Carbon Steel, 9 (2014) 2067–2079.

[52] W.C. Say, C.C. Chen, S.J. Hsieh, Electrochemical characterization of non-chromate surface treatments on AZ80 magnesium, Mater. Charact. 59 (2008) 1400–1406. doi:10.1016/j.matchar.2007.12.007.

[53] M. Babaei, C. Dehghanian, M. Vanaki, Effect of additive on electrochemical corrosion properties of plasma electrolytic oxidation coatings formed on CP Ti under different processing frequency, Appl. Surf. Sci. (2015). doi:10.1016/j.apsusc.2015.09.059.

[54] H. Duan, K. Du, C. Yan, F. Wang, Electrochemical corrosion behavior of composite coatings of sealed MAO film on magnesium alloy AZ91D, Electrochim. Acta. 51 (2006) 2898–2908. doi:10.1016/j.electacta.2005.08.026.

[55] M. Sabaghi Joni, A. Fattah-Alhosseini, Effect of KOH concentration on the electrochemical behavior of coatings formed by pulsed DC micro-arc oxidation (MAO) on AZ31B Mg alloy, J. Alloys Compd. 661 (2016) 237–244.

doi:10.1016/j.jallcom.2015.11.169.

[56] X. Tu, L. Chen, J. Shen, Y. Zhang, C. Miao, J. Wu, Effects of sucrose on anodized film formed on AZ31B magnesium alloy in environmental-friendly electrolyte, Int. J. Electrochem. Sci. 7 (2012) 9573–9579. doi:10.1016/j.jallcom.2009.04.053.

[57] U.M. Tefashe, P. Dauphin-ducharme, M. Danaie, Z.P. Cano, J.R. Kish, G.A. Botton, J. Mauzeroll, Localized Corrosion Behavior of AZ31B Magnesium Alloy with an Electrodeposited Poly (3 , 4-Ethylenedioxythiophene) Coating, 162 (2015) 536–544. doi:10.1149/2.0601510jes.

[58] M. Talha, Y. Ma, Y. Lin, A. Singh, W. Liu, X. Kong, Corrosion behaviour of austenitic stainless steels in phosphate buffer saline solution: synergistic effects of protein concentration, time and nitrogen, New J. Chem. 43 (2019) 1943–1955. doi:10.1039/C8NJ04670K.

[59] ISO, Document 10993-5, Biological evaluation of medical devices, Tests for Cytotoxicity: In Vitro Methods, Part 5, Int. Organ. Stand. Geneva, Switzerland (2009).

Table 1. Average roughness (Ra) of the AZ31B alloy in the polished and anodized.

Sample	Ra (μm)
Polished	0.07 ± 0.01
5 $mA.cm^{-2}$	2.65 ± 0.24
10 $mA.cm^{-2}$	2.24 ± 0.31
20 $mA.cm^{-2}$	2.80 ± 0.21

Table 2. XPS fitting parameters for the Si2p core levels of the anodized samples.

	5 $mA.cm^{-2}$		10 $mA.cm^{-2}$		20 $mA.cm^{-2}$	
Component	Sílica	Silicate	Sílica	Silicate	Sílica	Silicate
BE (eV)	104.1	102.6	----	102.4	----	102.0
FWHM (eV)	2.49	2.57	----	2.81	----	2.04
at.%	73.9	26.1	----	100	----	100

Table 3. Electrochemical parameters obtained from the potentiodynamic polarization

Condition	E_{corr} (mV vs. Ag/AgCl)	i_{corr} (μA.cm^{-2})	R_p (kΩ.cm^2)	b_a^{AZ31B}(mV.dec^{-1})	P (%)
Polished	-1407 ± 4	30.6 ± 8.4	0.720	100.34	–
5 mA.cm^{-2}	-1464 ± 91	3.7 ± 2.9	5.676	–	9.39
10 mA.cm^{-2}	-1455 ± 42	1.4 ± 0.6	38.20	–	0.98
20 mA.cm^{-2}	-1473 ± 70	2.0 ± 0.8	51.32	–	0.85

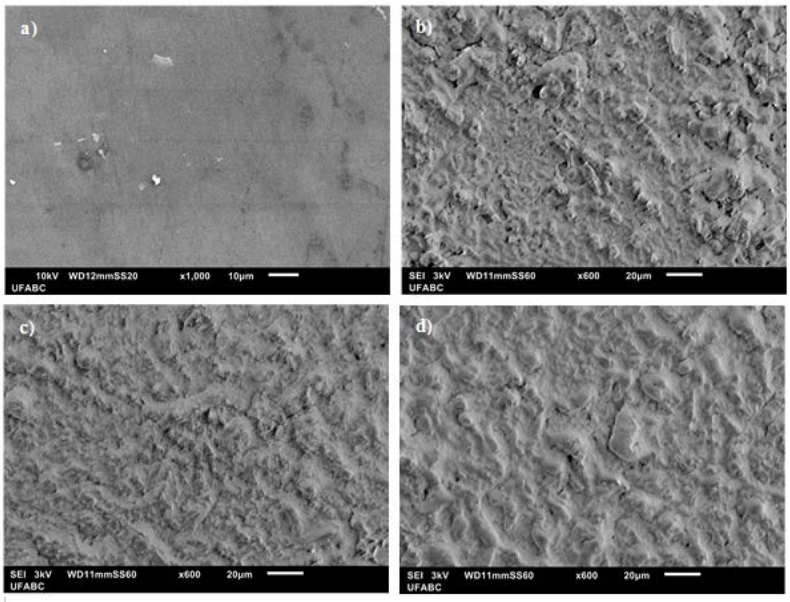

Figure 1. SEM images of the top surfaces of AZ31B alloy polished (a) and anodized in different current densities: b) 5 mA/cm^2; c) 10 mA/cm^2; d) 20 mA/cm^2.

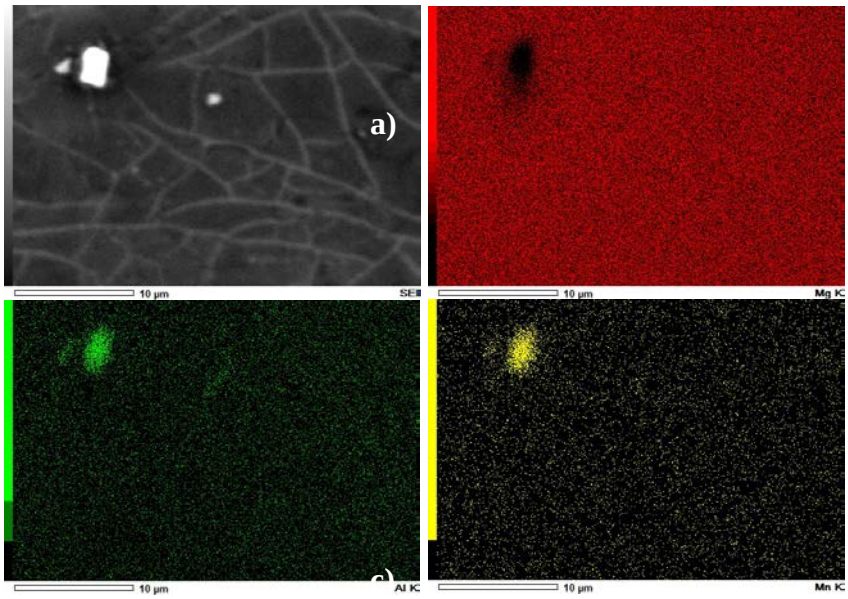

Figure 2. (a) Top surface of AZ31B alloy polished and EDS mapping of: (b) Mg; c) Al; d) Mn.

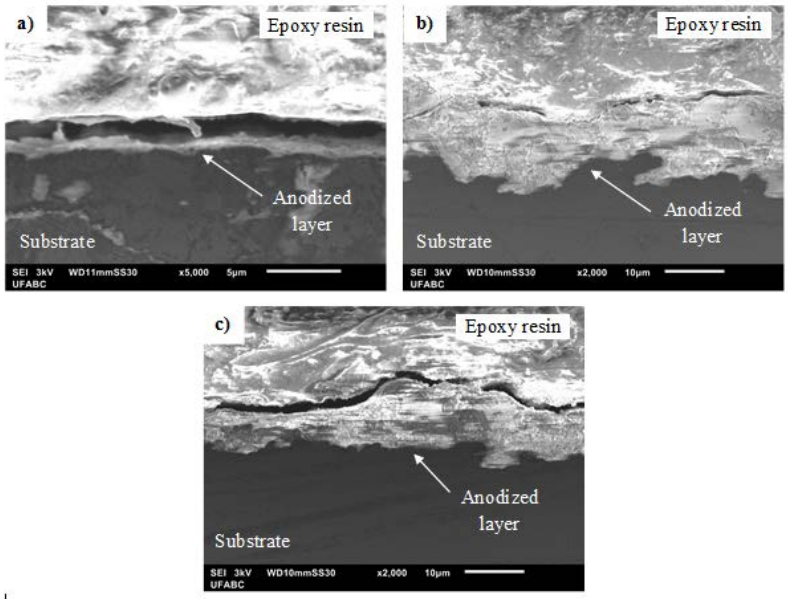

Figure 3. SEM cross-sectional images of the anodized AZ31B alloy in different current densities: a) 5 mA/cm^2; b) 10 mA/cm^2; c) 20 mA/cm^2.

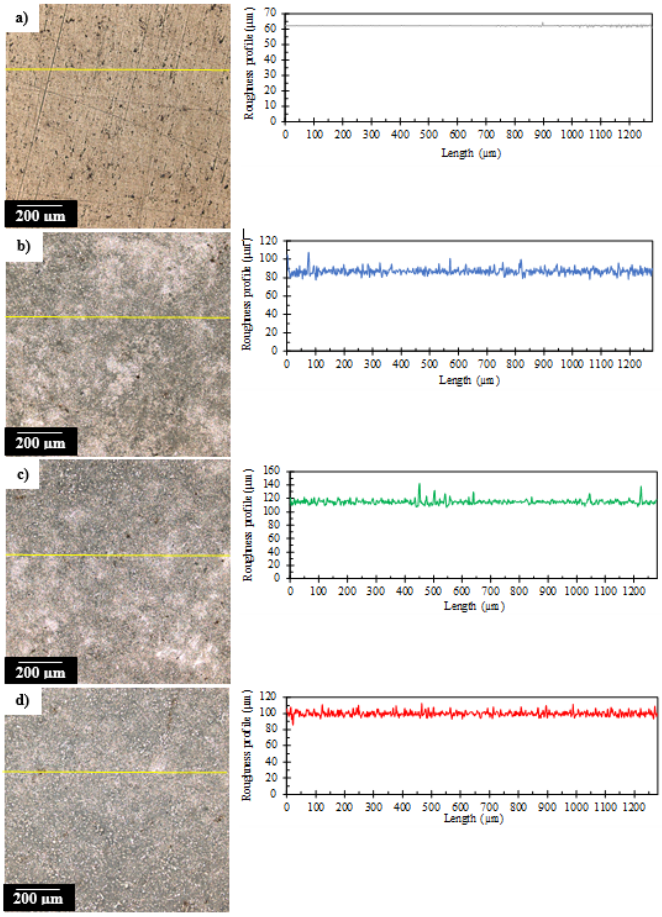

Figure 4. CLSM 2D images and roughness profile of AZ31B alloy polished (a) and anodized in different current densities: b) 5 mA/cm^2; c) 10 mA/cm^2; d) 20 mA/cm^2.

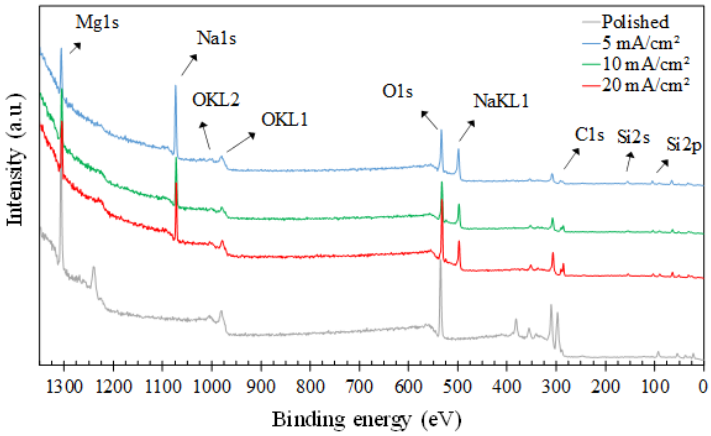

Figure 5. XPS survey spectra of the AZ31B alloy.

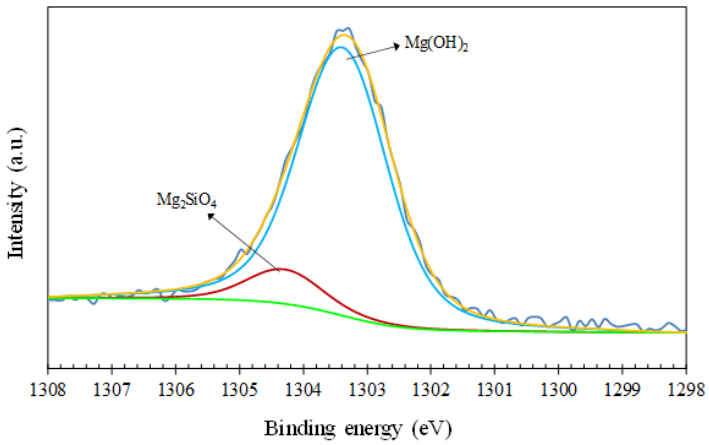

Figure 6. XPS Mg1s core level for the AZ31B alloy anodized at 20 mA.cm^{-2}.

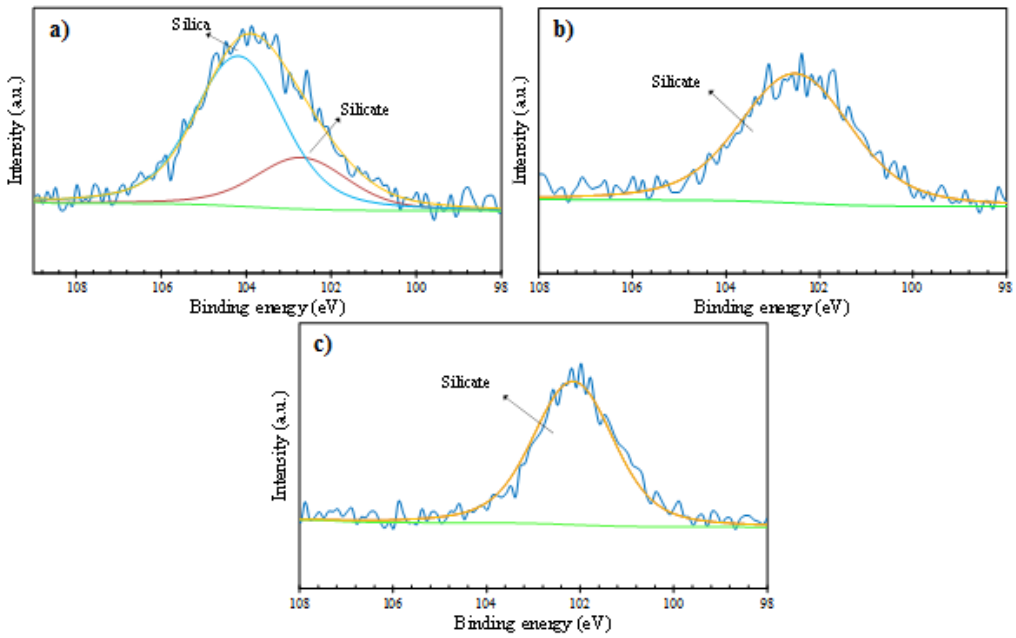

Figure 7. XPS Si2p core levels for the AZ31B alloy anodized at different current densities: a) 5 mA.cm^{-2}; b) 10 mA.cm^{-2}; c) 20 mA.cm^{-2}.

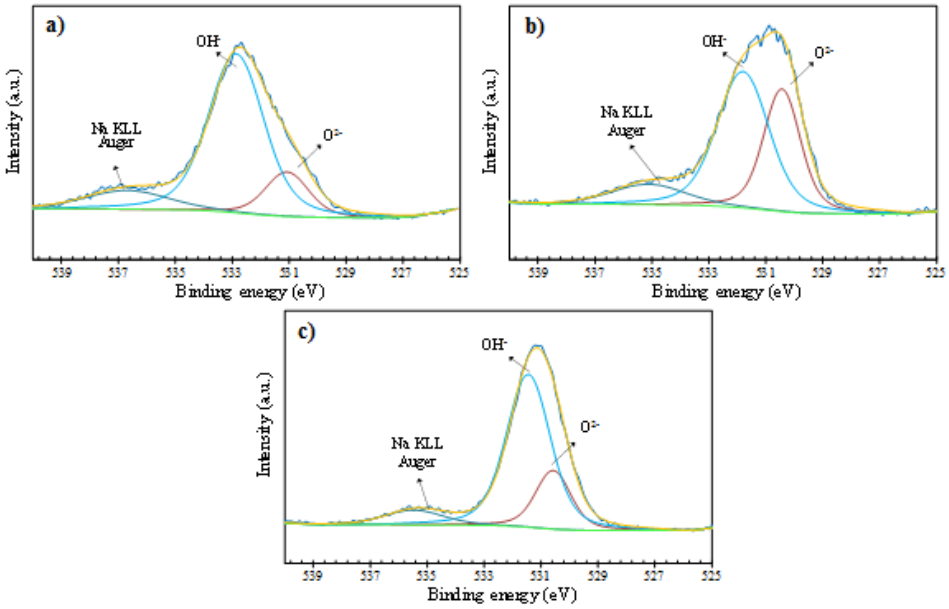

Figure 8. XPS O1s core levels for the AZ31B alloy anodized at different current densities: a) 5 mA.cm^{-2}; b) 10 mA.cm^{-2}; c) 20 mA.cm^{-2}.

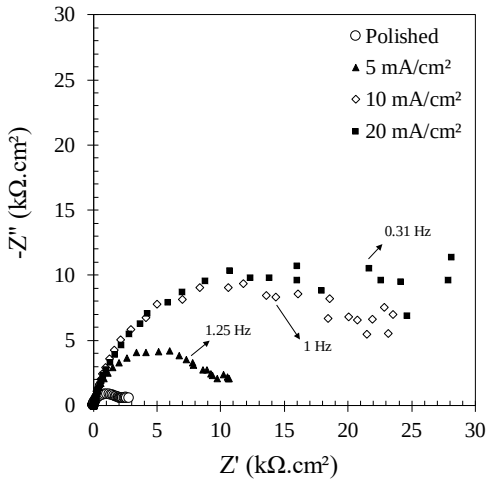

Figure 9. Nyquist plots of the polished and anodized AZ31B alloy. Electrolyte: PBS at room temperature.

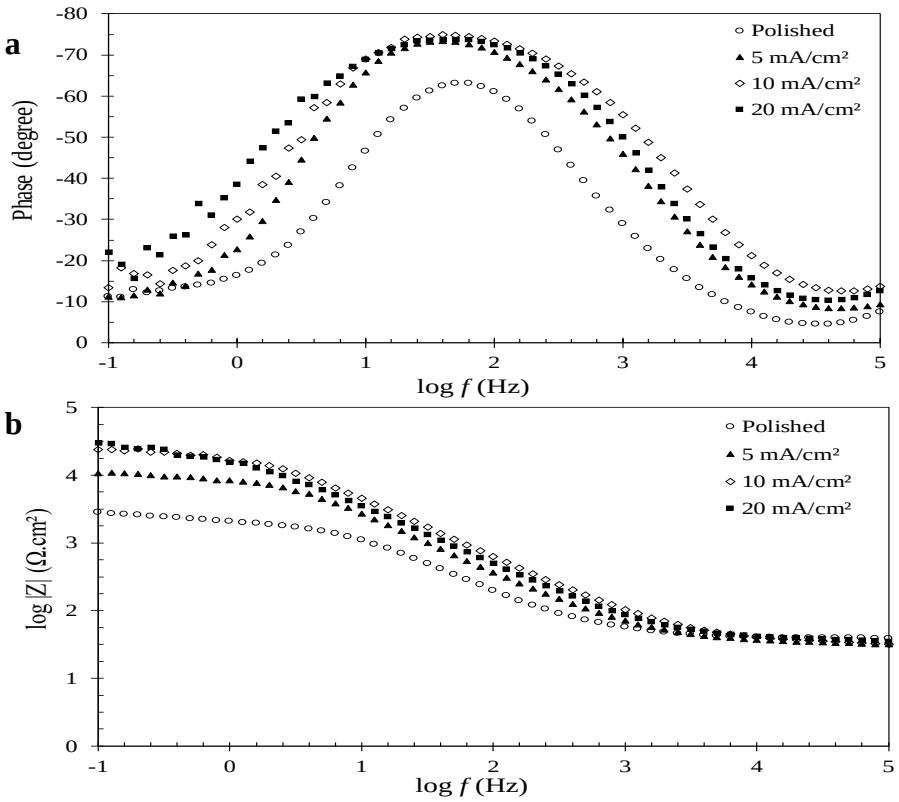

Figure 10. Bode plots of the polished and anodized AZ31B alloy: a) Phase plots; b) Impedance modulus vs. frequency plots. Electrolyte: PBS at room temperature.

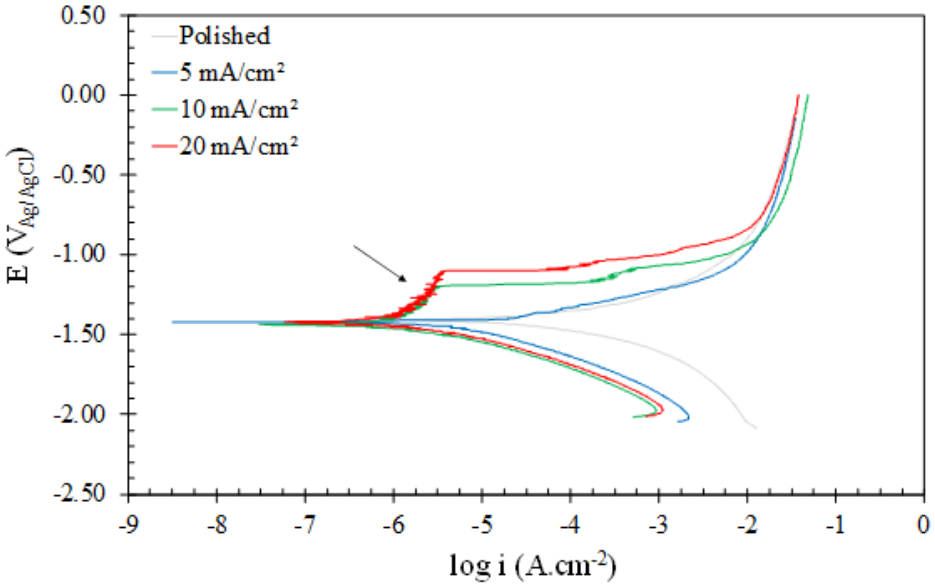

Figure 11. Potentiodynamic polarization curves of the polished and anodized AZ31B alloy in PBS at room temperature.

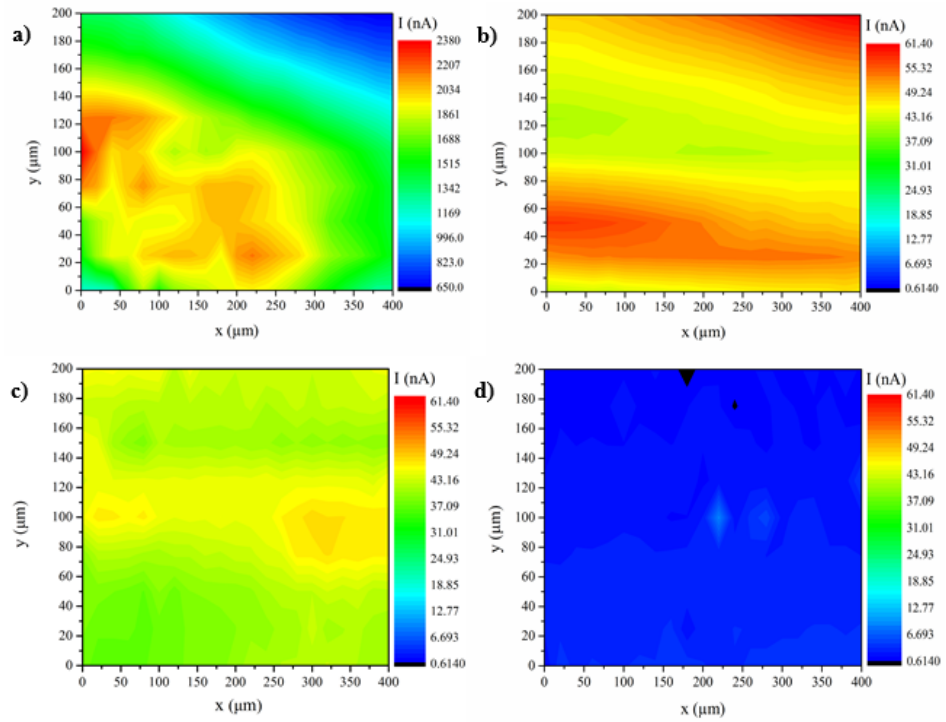

Figure 12. 2D SECM maps of H_2 evolution in SG/TC mode on the surface of AZ31B alloy polished (a) and anodized in different current densities: b) 5 mA.cm^{-2}; c) 10 mA.cm^{-2}; d) 20 mA.cm^{-2}. The anodized sample maps are in the same scale, except the polished condition (a) due its greater difference. Larger current, e.g. red domains, corresponds to higher flux of H_2.

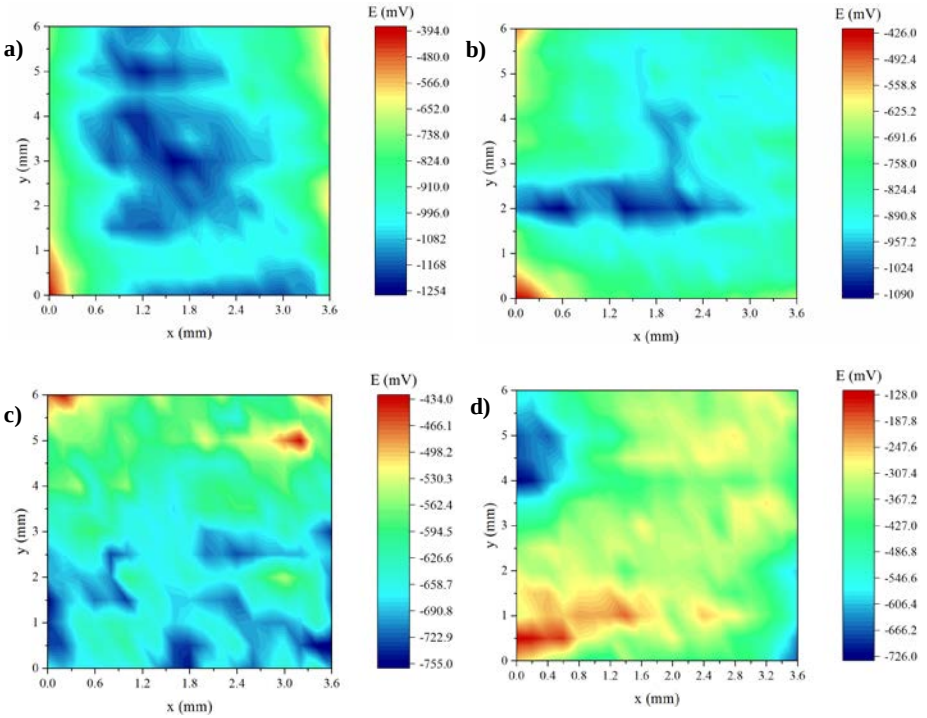

Figure 13. SKP surface distributions of AZ31B alloy polished (a) and anodized in different current densities: b) 5 mA.cm^{-2}; c) 10 mA.cm^{-2}; d) 20 mA.cm^{-2}. Anode regions, e.g. blue domains.

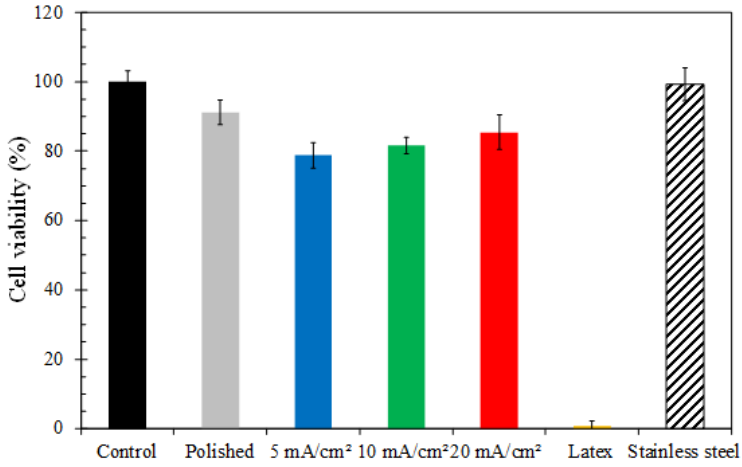

Figure 14. Cell viability of the control, polished and anodized AZ31B alloy.